

# Structure, chemistry and electrical properties of extended defects in crystalline silicon for photovoltaics

M. Seibt<sup>1,\*</sup>, D. Abdelbarey<sup>1</sup>, V. Kveder<sup>2</sup>, C. Rudolf<sup>1</sup>, P. Saring<sup>1</sup>, L. Stolze<sup>3</sup>, and O. Voß<sup>1</sup>

<sup>1</sup> IV. Physikalisches Institut der Georg-August-Universität Göttingen, Friedrich-Hund-Platz 1, 37077 Göttingen, Germany

<sup>2</sup> permanent address: Institute of Solid State Physics RAS, 142432 Chernogolovka, Russia

<sup>3</sup> now at: Q-Cells AG, Guardianstraße 16, 06766 Bitterfeld-Wolfen, Germany

Received 17 September 2008, revised 13 January 2009, accepted 14 April 2009

Published online 17 June 2009

PACS 61.72.J-, 61.72.Nn, 61.72.Yx, 64.75.Qr, 84.60.Jt

\* Corresponding author: e-mail seibt@ph4.physik.uni-goettingen.de, Phone: +49-551-394553, Fax: +49-551-394560

The electronic properties of present-day multicrystalline silicon (mc-Si) materials for photovoltaic applications are strongly influenced by point defects, their mutual interaction and their interaction with dislocations and grain boundaries. This paper presents results from fundamental investigations of metal impurity interaction with extended defects, namely a small-angle grain boundary and bulk microdefects. It is shown that the distribution of copper silicide precipitates closely follows the density of bulk microdefects indicating the underlying physics of 'good' and 'bad' grains frequently observed in mc-Si. Co-precipitation of copper and nickel in the same samples leads to virtually the same distribution of multi-metal silicide precipitates which according to light-beam

induced current measurements show the same recombination activity as single-metal silicide particles. Transmission electron microscopy is used to show that for copper-rich and nickel-rich conditions two types of silicides co-exist, i.e.  $\text{Cu}_3\text{Si}$  precipitates containing a small amount of nickel and  $\text{NiSi}_2$  precipitates containing some copper. Finally, phosphorus-diffusion gettering (PDG) is discussed as the main gettering process used in present-day silicon photovoltaics. Special emphasis is put on the effect of extended defects and their interaction with metal impurities on PDG kinetics. It is shown that different limiting processes will be simultaneously operative in mc-Si as a result of inhomogeneous bulk defect distributions.

© 2009 WILEY-VCH Verlag GmbH & Co. KGaA, Weinheim

**1 Introduction** The workhorse of present-day photovoltaics is crystalline silicon in the form of 180–300  $\mu\text{m}$  thick wafers with ongoing efforts to reduce the thickness in order to lower silicon material consumption. Besides monocrystalline materials grown by the Czochralski technique, a variety of growth techniques are currently used to produce multicrystalline silicon materials (mc-Si) with typical grain sizes in the *mm* and *cm* range (see [1] for a review). The latter include directional solidification (examples: Bridgman, and block casting [2,3]), ribbon growth (examples: edge-defined film fed growth, *EFG*, [4] and string ribbon, *SR*, [5]) as well as sheet growth (example: ribbon growth on substrate, *RGS*, [2,6]) and constitute more than 50% of present-day solar cell production [7]. Owing to this variety of growth techniques, the mate-

rials show somewhat unique microstructures rather than a typical defect spectrum.

Due to the fast increase of solar cell production exceeding a 30% annual growth and currently reaching 3GWp of annular solar cell installation [8] the supply of solar grade silicon feedstock has become a limiting factor of solar cell production. Since the standard Siemens process to purify metallurgical silicon is rather cost-effective, current efforts aim at using low-cost silicon feedstock such as solar grade polysilicon or upgraded polysilicon. These trends add to the significance of the topic of defects in silicon and their various interaction.

In general, all materials contain extended defects of intrinsic origin such as grain boundaries and dislocations. In addition, light element impurities such as carbon, nitrogen

and oxygen, are typical contaminants that result from reaction of the chemically aggressive silicon melt with the crucible. Carbon and nitrogen are known to form rod-like and filament-like precipitates consisting of SiC and Si<sub>3</sub>N<sub>4</sub>, respectively, which directly grow from the melt at the liquid/solid interface [9–11] and frequently give rise to local shunts in solar cell emitters [12]. Oxygen can be found as interstitial species and as silicon oxide precipitates that are frequently located at grain boundaries.

The electrical performance of such materials, i.e. mainly their minority carrier lifetime, is closely related to the presence of metal impurities introduced via the feedstock [1], during crystal growth mainly from the crucible [13] or during solar cell processing. Among the most prominent metal impurities are the 3d transition elements chromium, nickel, copper and in particular iron [14]. These impurities strongly interact with existing crystal defects to form complexes, accumulate at dislocations or grain boundaries in different forms [15,16], or even form silicide precipitates that, in general, simultaneously contain several metal impurities. The complex interaction of oxygen and metal impurities with extended defects in mc-Si has recently been shown by an impressive TEM study [17]. Segregation of point defects in the strain field of dislocations [18] and also their binding to the dislocation core [19] is another important topic in this context.

In order to gain control and reduce the level of metal impurities, gettering is routinely included into solar cell processing, in particular phosphorus-diffusion gettering (PDG) and aluminum gettering (AIG) [20,21]. For quantitative understanding and simulation of gettering schemes suitable to control metal impurities for the benefit of material properties their interaction with extended defects and with other metal or non-metal impurities have to be studied and described in terms of thermodynamic and kinetic models. In addition, the recombination properties of decorated crystal defects or multi-metal- precipitates have to be known if their effect on the material performance for photovoltaic applications is to be estimated.

This paper summarises recent experiments on metal impurity interaction with extended defects and its effect on gettering kinetics and efficiency. Section 2 is devoted to the effect of inhomogeneous densities of extended defects on the distribution of metal impurities. The competition of bulk microdefects and a small-angle grain boundary as efficient nucleation sites is studied in some detail for copper and for copper-nickel co-precipitation. In this context, experimental approaches to study the structure and chemistry of individual extended defects by TEM techniques are briefly discussed. Light-beam induced current (LBIC) studies show that extended defects forming in either case exhibit a very similar recombination activity.

The effect of extended defects on the kinetics of phosphorus-diffusion gettering, which is the most important gettering process in silicon photovoltaics, is discussed in Section 3 with special emphasis on the dissolution of metal

silicide precipitates (Section 3.1) and binding of impurities to dislocations (Section 3.2).

**2 Inhomogeneous defect density: effect on metal impurity distribution** Grain boundaries and dislocations are in general inhomogeneously distributed in mc-Si wafers due to ample time for their redistribution during crystal growth and, to a lesser extent, during solar cell processing. It has previously been recognized that the minority carrier lifetime in mc-Si wafers considerably degrades if high temperature annealing is finished by fast cooling to room temperature whereas slow cooling might even improve the material [22]. Obviously, metal impurities which are mainly gathered in precipitates at grain boundaries after crystal growth are (partly) released during annealing leading to the contamination of neighbouring grains at high temperature. If the cooling terminating the final processing step is sufficiently fast to prevent reprecipitation into large particles, the material might indeed degrade electronically. Such effects have been directly observed by means of x-ray fluorescence microscopy ( $\mu$ -XRF) [23].

A critical cooling rate leading to material degradation can not simply be concluded from general arguments since it can be influenced and possibly also limited by *impurity-related* and *material-related* parameters. Among others, we have

- the diffusion coefficient of the respective metal impurity,
- the concentration of the metal impurity defining the temperature  $T_{sup}$  where the solid solution of the impurity in silicon gets supersaturated,
- the density and type of bulk defects potentially acting as nucleation sites for precipitation,
- the presence of surface layers or internal sinks where metal impurities can accumulate at high temperature and during cooling.

For the experiments described below specially designed silicon samples have been used enabling to study the effect of grain boundaries, surface layers, bulk defects and the simultaneous presence of two metal impurities, namely copper and nickel.

**2.1 Microstructure of model samples** The materials used in our experiments were silicon bicrystals produced by wafer direct bonding under hydrophobic conditions [24]. The two starting wafers were (001) oriented n-type Czochralski-grown silicon with doping levels of  $2 \times 10^{14} \text{ cm}^{-3}$  (wafer A) and  $2 \times 10^{15} \text{ cm}^{-3}$  (wafer B).

Figure 1(a) schematically shows the microstructure of the bicrystals: The dislocation network at the bonding interface is indicated by the dashed-dotted line between the arrows. It consists of screw and edge dislocations with dislocation spacings of 12 nm and 372 nm, respectively. This interface with a Si (001) plane is subsequently referred to as a small-angle grain boundary, SAGB. As indicated, wafer B contained silicon oxide particles at a density of

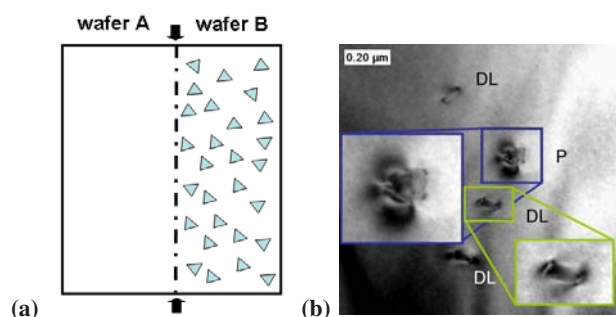


**Figure 1** (a) Schematic cross-section of the silicon bicrystal: wafer B contains bulk defects in a density of about  $10^{10} \text{ cm}^{-3}$ , whereas wafer A is virtually defect-free. The small-angle grain boundary (SAGB) is indicated by arrows and the dashed-dotted line. (b) TEM bright-field image of a silicon oxide precipitate (P) and punched-out dislocation loops (DL) observed in the bulk of wafer B.

about  $10^{10} \text{ cm}^{-3}$  whereas no such defects could be observed by TEM and defect etching in wafer A. A typical defect configuration is shown in Fig. 1(b): polyhedral silicon oxide precipitates associated with small dislocation loops which presumably have been punched out in order to relieve the misfit with the silicon matrix.

For single-metal in-diffusion experiments, nickel or copper was evaporated on one large surface of the bicrystal. Subsequent annealing was done at  $1050^\circ\text{C}$  for 30 minutes in Ar atmosphere and finished by moderately fast cooling at a rate of about 6 K/s. The same procedure was used for copper-nickel co-diffusion aside from the fact that one surface was covered by a thermally evaporated nickel film, the other with a copper film.

**2.2 Copper-silicide precipitate colonies** A single-metal diffusion experiment was performed using copper which is known to effectively decorate extended defects in silicon [25]. In order to study the large-scale defect distribution LBIC maps were measured in cross-section as well as preferential etching in the same geometry using Secco etch [26]. As an example, Fig. 2(a) shows a LBIC map which enables important conclusions about the defect distribution and nature. These are:

- A high density of extended recombination-active defects has formed in wafer B. They are well-known copper silicide colonies [27] which show very high LBIC contrasts [28] in agreement with previous electron-beam induced current studies [29].
- A precipitate-free zone has formed beneath the copper silicide layer which was deposited on the surface of wafer B. Such a zone is absent in experiments with the copper film deposited on wafer A. Hence, the copper silicide layer effectively removes the copper from the silicon material during cooling. This process has been termed ‘self-gettering’ for the case of nickel in silicon [30] and is simply due to the fact that the copper sili-

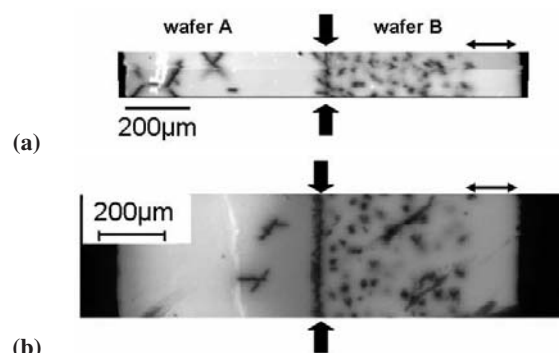


**Figure 2** Light-beam induced current maps obtained in cross-section along Si [110] of a bicrystal of copper diffusion (a) and copper-nickel co-diffusion (b) which show qualitatively identical defect distributions. A high density of recombination-active defects can be seen in wafer B (right-hand side) whereas only a few very large defects are obtained in wafer A. In addition, a precipitate-free zone (double-headed arrows) is observed in wafer B below the copper-silicide film. It should be noted that no precipitate-free zone has formed in wafer B close to the SAGB; the position of the latter is indicated by thick arrows.

cide establishes the copper solubility at the interface during cooling. Hence, it might be visualized as a very large precipitate without the necessity of nucleation.

- Only a few large defects have formed in wafer A indicating that the majority of copper atoms have diffused out to the backside and to the precipitates forming at the SAGB and inside wafer B.
- No precipitate-free zone has formed in wafer B close to the SAGB. This provides evidence that bulk defects – oxide particles and punched-out dislocations – act as very efficient nucleation sites obviously outperforming the SAGB. The latter contains screw and edge dislocations in a high density thus potentially providing similar nucleation sites as the bulk defects. Hence, quantitative arguments including numerical simulations of precipitation at different defects are needed to explain this observation; such simulation studies are presently performed.

**2.3 Co-precipitation of nickel and copper** Copper and nickel have been co-diffused from the two opposite large surfaces of the bonded wafer as described above. Under such conditions, according to solubility data obtained for the respective binary system [32] the copper concentration in the wafer exceeds that of nickel so that copper-rich conditions are always established (Section 2.3.1). In a second set of experiments nickel-rich conditions have been established by only partially covering the surfaces with the two metals and investigating areas remote from the edges of the copper film (Section 2.3.2).

**2.3.1 Copper-rich conditions** The LBIC map of the co-diffused copper-rich sample is shown in Fig. 2(b).

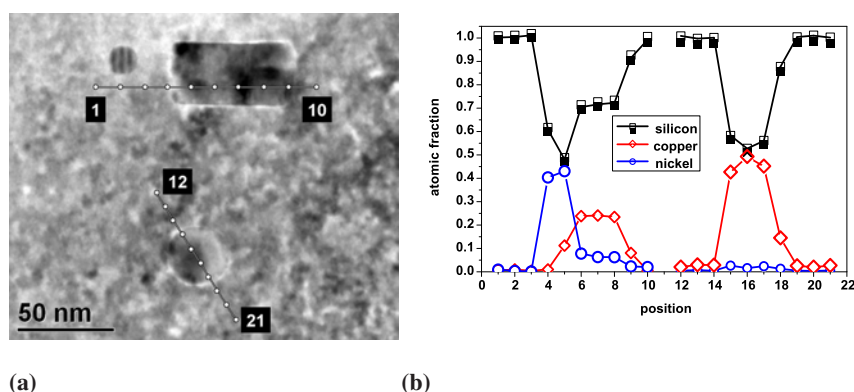


**Figure 3** X-ray analysis of particles inside a mixed copper-nickel-silicide colony. (a) High-resolution electron micrograph of three particles imaged along the Si  $[1\bar{1}2]$  zone axis; the lines and numbers refer to electron probe positions for EDX analysis shown in (b); the FWHM of the probe was 1 nm. (b) Compositions at points indicated in (a) obtained from EDX spectra and their analysis using the method of Cliff-Lorimer [31]. Points 12 to 21 go across a Cu-rich precipitate whereas points 1 to 10 are located across a Ni-rich precipitate directly attached to a copper-rich particle.

Compared to the case of only copper contamination (Fig. 2(a)) one can state the following:

- The overall defect distribution is the same in copper-diffused and copper-nickel co-diffused samples.
- The recombination activity of defects formed as a result of co-precipitation is virtually the same as that in the case of pure copper silicide colonies. This view is confirmed by quantitative LBIC analysis part of which has been published recently [28].

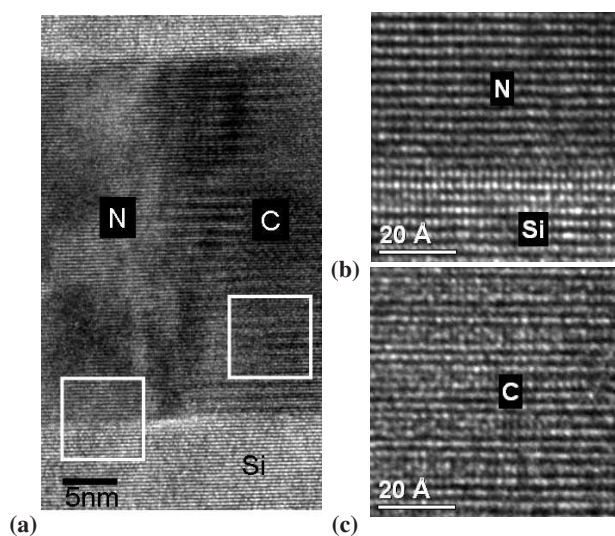


**Figure 4** HRTEM image obtained along the Si  $[1\bar{1}2]$  zone axis of the combined silicide precipitate shown in Fig. 3. (a) Region showing the transition from the nickel-rich part (N) to the copper-rich part (C); white squares indicate positions of the magnified images shown in (b) and (c). (b) Magnified part from the nickel-rich part showing a lattice image typical for the cubic  $\text{NiSi}_2$  structure. (c) Magnified part from the copper-rich part showing additional Moiré fringes.

Extensive TEM analyses provide a consistent picture of the defects forming if copper and nickel co-precipitate under copper-rich conditions [33]. Briefly, particle colonies

are observed which simultaneously contain copper-rich silicide precipitates containing a few at% of nickel and nickel-rich silicide precipitates that contain some copper. As an example obtained from investigations of a TEM lamella prepared as described in [34], Fig. 3(a) provides a high-resolution electron (HRTEM) micrograph taken from the interior of a colony. It shows three distinct precipitates with typical sizes between 10 and 70 nm. The two circular particles mainly contain copper as is revealed by EDX analysis (Fig. 3(b), points 12 to 21). The data further show that the partial mole fraction  $X_{\text{Ni}}$  of nickel is less than 3%, where

$$X_M = \frac{c_M}{c_{\text{Ni}} + c_{\text{Cu}}}, \quad (\text{M}=\text{Ni,Cu}), \quad (1)$$

while  $c_{\text{Ni}}$  and  $c_{\text{Cu}}$  refer to nickel and copper concentrations (in at%), respectively, as measured by EDX. Statistical analysis of EDX data obtained from a large number of such precipitates reveals an average value of  $X_{\text{Ni}} = (4.6 \pm 0.3)\%$  for the partial mole fraction [33].

The nickel-rich precipitate at the top of Fig. 3(a) is directly attached to a copper-rich region as can be seen from points 1 to 10 shown in Fig. 3(b). It should be noted, that in addition to such configurations of copper-rich and nickel-rich particles sitting 'back-to-back' also isolated nickel-rich precipitates of the same size are observed inside the colonies [33]. Their crystal structure can be deduced from HRTEM images as being that of the cubic  $\text{NiSi}_2$ .

An example is given in Fig. 4 showing HRTEM images of the interface region between the nickel- and copper-rich parts of the precipitate chemically analysed in Fig. 3(b). In Fig. 4(a) of that image the nickel-rich region (N) exhibits the lattice image as the silicon matrix which is imaged along the  $[1\bar{1}2]$ - direction; an enlarged portion is provided in Fig. 4(b). Such appearance is typical for the cubic  $\text{NiSi}_2$  implying that nickel-rich precipitates and nickel-rich parts of precipitates consist of a solid solution of copper in  $\text{NiSi}_2$ , subsequently referred to as  $\text{NiSi}_2\text{:Cu}$ . The maximum copper content of these precipitates corresponds to a partial mole fraction of  $X_{\text{Cu}} = 25\%$ , the average value is  $X_{\text{Cu}} = (23 \pm 5)\%$  [33].



The copper-rich part marked as 'C' in Figs. 4(a) and (c) clearly shows Moiré fringes and is consistent with the  $\text{Cu}_3\text{Si}$  phase containing a certain amount of nickel like their isolated counterparts (points 12 to 21 in Fig. 3). Please note, that the extraordinarily high nickel content indicated by points 6 to 8 in Fig. 3(b) presumably arises from the overlap of nickel- and copper-rich precipitate parts along the electron beam.

**2.3.2 Nickel-rich conditions** For nickel-rich conditions much smaller etch-pits and LBIC contrasts (not shown) are observed. The rather small defect density in this case made a traditional TEM sample preparation rather difficult so that the focused-ion beam (FIB) technique in combination with defect delineation by preferential chemical or ion-beam etching was applied [34]. The result of a successful preparation using very short preferential etching is shown in Fig. 5(a). The encircled region shows the original etch-pit used to localise the SAGB and the defects attached to it. It is now filled with the C:Pt composite typically used to protect the surface during FIB operation. In addition, the SAGB can be seen as a line contrast running through the whole lamella. Furthermore, a plate-shaped defect seemingly not attached to the SAGB is clearly visible as a dark line with the size of about  $1.5\ \mu\text{m}$ .

The main features of these defects are summarised in Fig. 5(b) which is a bright-field image obtained from one end of the platelet. Strong punching of dislocations (D) is easily recognised together with copper-rich precipitates inside the platelet (C1) and attached to dislocations in the silicon matrix (C2).

The other end of the platelet is analysed in some detail in Fig. 6. Part (a) is a bright-field image again showing severe dislocation punching and copper-rich particles (C) inside the platelet. The most left-hand precipitate is chemically analysed as shown in part (b) of that figure: the copper-rich precipitate has an interface with the silicon which is inclined with respect to the electron beam. Hence, the precipitate fraction of the total foil thickness increases almost linearly with position between 0 and about 140 nm in the linescan shown in Fig. 6(b). Here, the copper signal increases almost linearly which is accompanied by an almost linear *decrease* of the silicon signal before normalisation (not shown). The latter provides evidence that silicon atoms have been emitted from this copper-rich region which is typical if precipitates of the  $\text{Cu}_3\text{Si}$  phase form. It should be noted that the nickel content in this part corresponds to a partial mole fraction of  $X_{\text{Ni}} \simeq 2.7\%$  which is close to the value found for copper-rich conditions (see Section 2.3.2). Please note that tilting experiments and EDX data consistently show that the plate-shaped precipitate runs through the whole TEM foil.

A final noteworthy observation can be made in Fig. 6(b) in the interior of the  $\text{NiSi}_2\text{:Cu}$  platelet, i.e. for positions above about 180 nm. This part shows an almost homogeneous copper content corresponding to a partial mole fraction of  $X_{\text{Cu}} = (18 \pm 3)\%$  which is - again - close

to the value obtained for copper-rich conditions. The homogeneity and the simultaneous presence of  $\text{NiSi}_2\text{:Cu}$  and  $\text{Cu}_3\text{Si}\text{:Ni}$  precipitates indicates that equilibrium has been established at some temperature during cooling between the solid solution of copper in the  $\text{NiSi}_2\text{:Cu}$  and the copper-rich precipitates inside the large platelet.

### 3 Implications for phosphorus-diffusion gettering

The main gettering technique used in silicon photovoltaics is phosphorus-diffusion gettering (PDG). This is mainly due to the fact that P diffusion is an integral part of solar cell processing which produces the highly n-doped emitter of a solar cell produced on p-doped crystalline silicon. In addition, aluminum gettering (AlG) is a possible candidate for efficiently removing metal impurities from crystalline silicon [35]. Technologically, however, the potential of AlG is not exploited during solar cell processing since typical conditions for back contact firing and backsurface field formation are not optimised in terms of gettering.

In the following, we will consider two phenomena related to the effect of extended defects on PDG kinetics and efficiency, namely the dissolution of metal silicide precipitates and the accumulation of metal impurities at dislocations.

#### 3.1 Dissolution of metal silicide precipitates

Transition metal impurities in crystalline silicon will predominantly precipitate if impurity atoms are sufficiently mobile when their solid solution in silicon gets supersaturated. Hence, for a given impurity its concentration and the thermal history of the material will determine the amount of precipitation. In addition, as we have seen in Section 2, density and type of pre-existing extended defects – grain boundaries, dislocations, bulk microdefects – strongly affect the metal distribution in inhomogeneous materials such as mc-Si for photovoltaics. These considerations hold for conditions typical in solar cell processing and also for typical conditions of crystal growth where the fast diffusors have ample of time to redistribute even on a large scale.

The main effect of pre-existing metal silicide precipitates on PDG kinetics is their *dissolution* which can be the rate-limiting step. This is illustrated in Fig. 7 which summarises part of the results of an extensive simulation study using the model described in [37] and extended to precipitated impurities as described in [21]. The simulations have been performed for a model impurity described in detail in [21]. Briefly, the impurity is assumed to have a diffusion coefficient and solubility in intrinsic silicon equal to those of interstitial iron. The acceptor levels of the respective substitutional species and its binding energy with phosphorus have been adjusted to experimental data for PDG of cobalt [36]. Furthermore, an initial impurity concentration of  $10^{14}\ \text{cm}^{-3}$  is assumed and a target concentration of  $10^{12}\ \text{cm}^{-3}$  to be reached at the end of the PDG process.

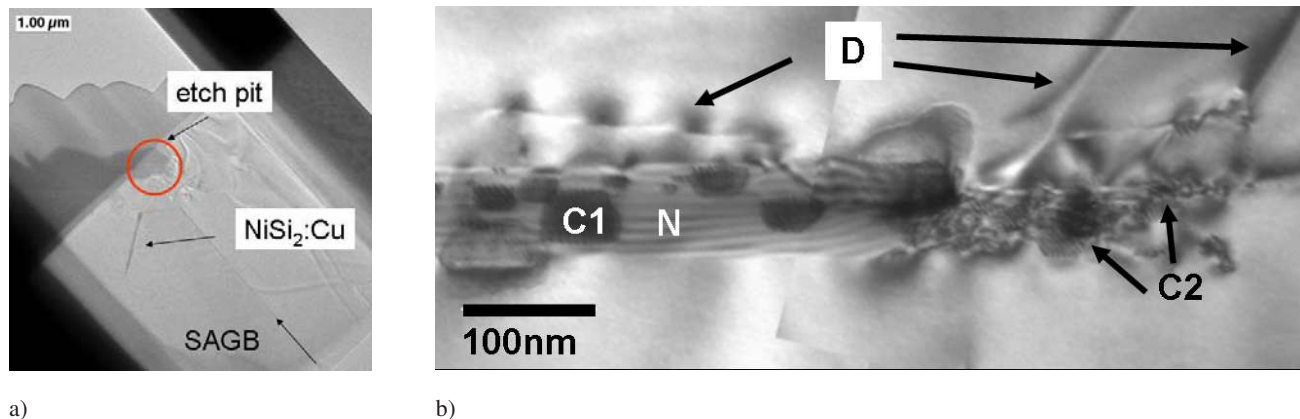


**Figure 5** Typical defect configuration obtained under nickel-rich conditions imaged along the Si  $[1\bar{1}0]$  zone axis. (a) Low-magnification TEM micrograph showing the surface etch-pit (circle) used to localise the defect for FIB preparation (see [34] for details), the grain boundary (SAGB) and a plate-shaped precipitate viewed edge-on ( $\text{NiSi}_2\text{:Cu}$ ). (b) Bright-field image of one end of the platelet showing the main features of these defects: a nickel-rich platelet (N) containing copper-rich precipitates (C1), punched-out dislocations (D) and copper-rich precipitates attached to punched-out dislocations in the silicon matrix (C2).

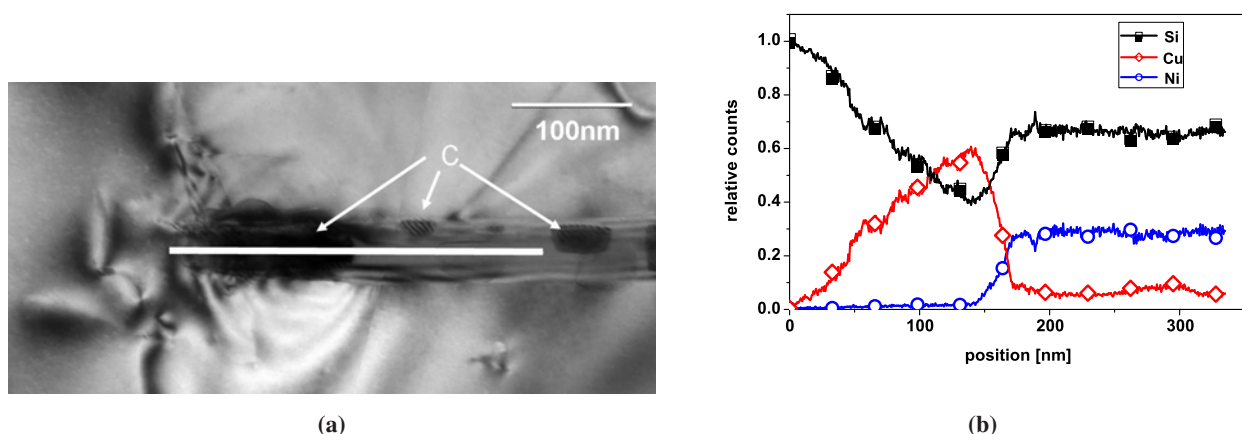


**Figure 6** Structural and chemical TEM analysis of the end-part of the  $\text{NiSi}_2\text{:Cu}$  platelet viewed edge-on in a  $[1\bar{1}0]$  oriented silicon foil. (a) Bright-field image showing dislocations in the silicon matrix punched out by the  $\text{NiSi}_2\text{:Cu}$  platelet which contains copper-rich precipitates (C). (b) Chemical analysis along the line shown in (a); the left-hand part shows a copper-rich region with an inclined interface to the silicon matrix giving rise to the almost linear increase of the copper signal accompanied by the almost linear decrease of the silicon signal. Please note the almost constant copper signal in the  $\text{NiSi}_2\text{:Cu}$  platelet.

The following considerations remain valid for other sets of parameters, the specific numbers, however, will change.

Figure 7 shows the gettering time  $t_g$  needed to reach the target concentration as a function of the gettering temperature,  $T_g$ . It can be seen that  $t_g$  has a pronounced minimum at about  $T_g = 900^\circ\text{C}$  if precipitates are present. This is easily understood taking into account that the solubility of the model impurity at about  $900^\circ\text{C}$  corresponds to the initial impurity concentration of  $10^{14}\text{ cm}^{-3}$ . Hence, the optimal gettering temperature  $T_g^{\text{opt}}$  is defined by the temperature where the initial impurity concentration is equal to the solid solubility of the impurity in intrinsic silicon. Below this temperature, precipitates will not completely

dissolve and act as a persistent source of impurities during PDG, i.e. in this regime PDG kinetics are limited by precipitate dissolution. Above this temperature, all precipitates will quickly dissolve at the onset of PDG in accord with the observation that  $t_g$  becomes independent of the precipitate density in this regime. Here, kinetics are limited by the formation of the highly phosphorus doped layer, i.e. by phosphorus in-diffusion [16]. The reason for this lies in the fact that the segregation effect of the highly P-doped layer strongly decreases with increasing temperature so that a much thicker P-doped layer is needed for the same amount of metal impurities to be accumulated there.

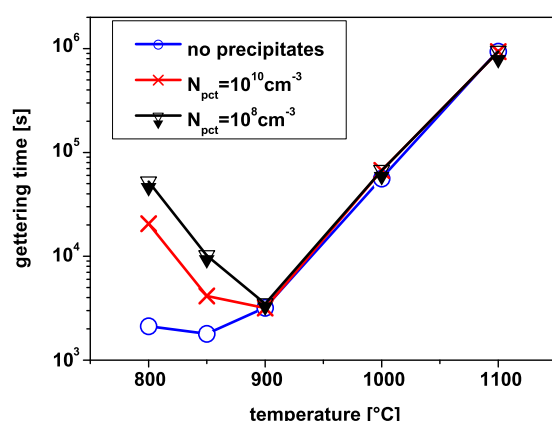


**Figure 7** Results of PDG simulations for a model impurity having the properties of iron in intrinsic silicon and properties in highly P-doped silicon as determined in [36].

Coming back to the results obtained for the bonded wafers which mimic the situation in mc-Si with its inhomogeneous distribution of dislocations (see Section 2) one has to conclude that both limiting regimes are simultaneously operative in typical mc-Si wafers: 'good' grains with a low density of dislocations and precipitates (wafer A in our experiments) will be in the P-diffusion-limited regime while in 'bad' grains precipitate dissolution will be incomplete and slow down the kinetics (dissolution-limited regime). Transferred to typical processing conditions – fixed  $t_g$  at a pre-defined  $T_g$  – this implies that 'good' grains will improve further even beyond a certain target value for the remaining impurity concentration while 'bad' grains scarcely improve or even degrade during PDG.

The main conclusions drawn in this section remain valid if more than one metal impurity is present in the material, i.e. if multi-metal silicides have formed. One should, however, keep in mind that the solid solubility of an impurity in a ternary or even quaternary system, in general, will be different from that in the binary system. In addition, new phenomena will arise in situations where the fast diffusing components of a multi-metal precipitates are quickly removed by gettering leaving behind the slower moving species which possibly can poison the material.

### 3.2 Accumulation of dissolved metal impurities at dislocations

The interaction of point defects with dislocations in silicon and its effect on the electronic structure of dislocations is a long-studied topic which has been reviewed recently [38]. Most important for crystalline silicon materials used in photovoltaics is the strong effect of deep level impurities close to or in the core of dislocations on the recombination properties of dislocations [16, 39]. Here, we will restrict the discussion to possible effects of accumulation of impurities at dislocations on gettering kinetics leaving aside electronic effects.

Apart from impurity precipitation at dislocations two basic mechanisms of impurity interaction with dislocations have to be considered, i.e. impurity segregation in the strain-field and 'chemical' binding to the dislocation core. For the former, maximum binding energies  $E_b$  of 0.8 eV have been estimated for an impurity such as substitutional gold [18] whereas up to 2.1 eV have been calculated for copper atoms in the core of glide dislocations [19]. The impact on gettering kinetics will be completely different, since the predominant fraction of impurities will be dissolved in the bulk for  $E_b = 0.8$  eV at a gettering temperature of 850 °C implying no effect on PDG kinetics whereas  $E_b = 2$  eV might lead to a considerable immobilisation the magnitude of which depends on the dislocation density and impurity concentration (see Fig. 8).

Evidence for an enhanced solubility for gold in silicon has been reported for polycrystalline silicon [40] and for highly dislocated silicon [41] deduced from radiotracer experiments. In addition, the formation of gold precipitates in highly dislocated silicon apparently forming *at in-diffusion temperature* has been observed by TEM [41] which has recently been confirmed in our group. This intriguing observation has not been discussed so far let alone been explained. It shows, however, that new phenomena occur in dislocated silicon that need further investigations.

**4 Conclusions** In summary, we have described results obtained for copper and nickel precipitation in silicon bicrystals produced from two different Czochralski grown wafers containing bulk defects at different densities and separated by a dislocation network constituting a small-angle grain boundary. Virtually identical precipitate distributions and recombination activities of precipitates are found for copper-diffused and copper-nickel co-diffused samples. In co-diffused samples  $\text{Cu}_3\text{Si:Ni}$  and  $\text{NiSi}_2\text{:Cu}$  silicide precipitates co-exist for both copper- and nickel-rich conditions. In addition, the chemical composition of each precipitate type is similar for copper- and nickel-rich conditions although the precipitate microstructure seems to follow that known for the dominating impurity in the respective binary case. Finally, the effect of extended defects on the kinetics of gettering, mainly phosphorus-diffusion gettering, has been demonstrated by means of simulation results. For precipitated metal impurities and those bound to dislocations as a point defect, the kinetics considerably slow down since the impurity is present in part as an immobile species.

**Acknowledgements** This work was financially supported by the German Federal Ministry for the Environment, Nature Conservation and Nuclear Safety and all the industry partners within the research cluster SolarFocus (0327650 B). The content of this publication is the responsibility of the authors. One of us (D.A.) gratefully acknowledges a scholarship of the Egyptian government. The authors are grateful to B. Schlieper-Ludewig and V. Radisch for technical support and to Th. Wilhelm and M. Reiche for providing the bonded wafer material.

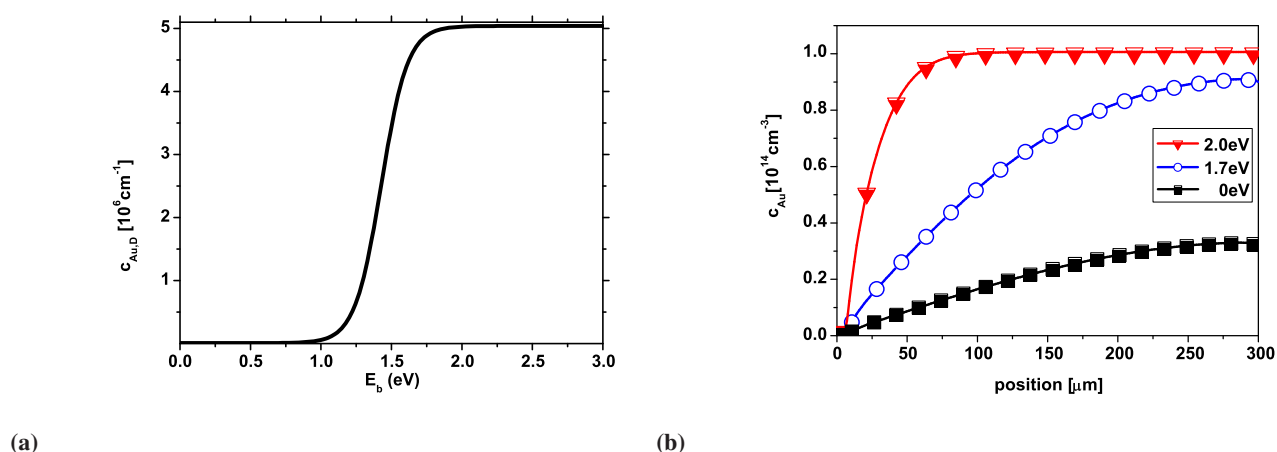


**Figure 8** Calculations for the binding of gold to the core of dislocations (dislocation density:  $10^8 \text{ cm}^{-2}$ , total gold concentration:  $5 \times 10^{14} \text{ cm}^{-3}$ ). (a) line concentration of gold (per dislocation length) at  $T = 800 \text{ }^\circ\text{C}$  as a function of the binding energy  $E_b$ ; please note, that virtually no binding occurs for  $E_b = 0.8 \text{ eV}$  whereas almost complete binding is observed above  $E_b = 1.7 \text{ eV}$ . (b) Effect of the binding energy on PDG kinetics at  $800 \text{ }^\circ\text{C}$ .

## References

- [1] W. Koch, A. L. Endrös, D. Franke, C. Häbeler, J. P. Kaleijs, and H. J. Müller, Handbook of Photovoltaic Science and Engineering, A. Luque and S. Hegedus (eds.) (John Wiley & Sons, 2005), chap. 6: Bulk Crystal Growth and Wafering for PV, p. 205.
- [2] A. Schönecker, I. J. Geerligs, and A. Müller, Solid State Phenom. **95/96**, 149 (2004).
- [3] T. F. Cizek, Crystal Growth Technology, H. J. Scheel and T. Fukuda (eds.) (John Wiley & Sons, Ltd.: Sussex, UK 2003), chap. Dislocations, p. 267.
- [4] J. P. Kaleijs, Solid State Phenom. **95/96**, 159 (2004).
- [5] J. I. Hanoka, Sol. Energy Mater. Sol. Cells **65**, 231 (2001).
- [6] G. Hahn and A. Schönecker, J. Phys.: Condens. Matter **16**, R1615 (2004).
- [7] H. Matsuo, R. Ganesh, S. Nakano, L. Liu, K. Arafune, Y. Ohshita, M. Yamaguchi, and K. Kakimoto, J. Cryst. Growth **310**, 2204 (2008).
- [8] D. Ginley, M. A. Green, and R. Collins, MRS Bull. **33**, 355 (2008).
- [9] H. J. Möller, Solid State Phenom. **95/96**, 181 (2004).
- [10] J. Bauer, O. Breitenstein, and J. P. Rakotoniaina, Phys. Status Solidi A **204**, 2190 (2007).
- [11] J. Bauer, O. Breitenstein, A. Lotnyk, and H. Blumtritt, Proc. 22nd European Photovoltaic Solar Energy Conference, 3-7 September 2007, Milan, Italy, 2007.
- [12] O. Breitenstein, J. Bauer, T. Trupke, and R. A. Bardos, Prog. Photovolt: Res. Appl. **16**, 325 (2008).
- [13] T. Buonassisi, A. Istratov, M. Pickett, J. P. Rakotoniaina, O. Breitenstein, M. Marcus, S. Heald, and E. Weber, J. Cryst. Growth **287**, 402 (2006).
- [14] T. Buonassisi, A. A. Istratov, M. D. Pickett, M. Heuer, J. P. Kaleijs, G. Hahn, M. A. Marcus, B. Lai, Z. Cai, S. M. Heald, T. F. Cizek, R. F. Clark, D. W. Cunningham, A. M. Gabor, R. Jonczyk, S. Narayanan, E. Sauar, and E. R. Weber, Prog. Photovolt: Res. Appl. **14**, 513 (2006).
- [15] M. Seibt, V. Kveder, W. Schröter, and O. Voß, Phys. Status Solidi A **202**(5), 911 (2005).
- [16] M. Seibt, R. Khalil, V. Kveder, and W. Schröter, Appl. Phys. A, in press (2009); DOI: 10.1007/s00339-008-5027-8.
- [17] H. Nordmark, M. D. Sabatino, E. J. O. vrelid, J. C. Walmsley, and R. Holmestad, Proceedings 22nd EUPVSEC, 3-7 Sept. 2007, Milan, Italy p. 1710 (1971).
- [18] R. Bullough and R. C. Newman, Prog. Semicond. **7**, 100 (1963).
- [19] N. Fujita, R. Jones, S. Öberg, P. Briddon, and A. Blumennau, Solid State Phenom. **131-133**, 259 (2008).
- [20] S. M. Myers, M. Seibt, and W. Schröter, J. Appl. Phys. **88**, 3705 (2000).
- [21] M. Seibt, A. Sattler, C. Rudolf, O. Voß, V. Kveder, and W. Schröter, Phys. Status Solidi A **203**, 696 (2006).
- [22] M. Seibt, M. Apel, I. Hanke, and W. Schröter, Proc. 6th Workshop on the Role of Impurities and Defects in Silicon Device Processing (NREL/SP-413-21551) p. 118 (1996).
- [23] T. Buonassisi, A. A. Istratov, S. Peters, C. Ballif, J. Isenberg, S. Riepe, W. Warta, R. Schindler, G. Willeke, Z. Cai, B. Lai, and E. R. Weber, Appl. Phys. Lett. **87**, 121918 (2005).
- [24] M. Reiche, Phys. Status Solidi A **203**, 747 (2006).
- [25] W. C. Dash, J. Appl. Phys. **27**, 1193 (1956).
- [26] F. S. d'Aragona, J. Electrochem. Soc. **119**, 948 (1972).
- [27] E. Nes and J. Washburn, J. Appl. Phys. **42**, 3526 (1971).
- [28] P. Saring, C. Rudolf, L. Stolze, and M. Seibt, Mater. Sci. Eng. B, accepted for publication (2009).
- [29] M. Kittler, C. Ulhaq-Bouillet, and V. Higgs, J. Appl. Phys. **78**, 4573 (1995).
- [30] N. Gay and S. Martinuzzi, Appl. Phys. Lett. **70**, 2568 (1997).
- [31] G. Cliff and G. W. Lorimer, J. Microsc. **103**, 203 (1975).
- [32] E. R. Weber, Appl. Phys. A **30**, 1 (1983).
- [33] C. Rudolf, P. Saring, L. Stolze, and M. Seibt, Mater. Sci. Eng. B **159/160**, 365 (2009).



- [34] L. Stolze, C. Rudolf, P. Saring, and M. Seibt, *Phys. Status Solidi C* **6**(8), 1862 (2009), this issue.
- [35] L. Verhoef, P. Michiels, S. Roorda, and W. Sinke, *Mater. Sci. Eng. B* **7**, 49 (1990).
- [36] W. Schröter, V. Kveder, M. Seibt, A. Sattler, and E. Spiecker, *Sol. Energy Mater. Sol. Cells* **72**, 299 (2002).
- [37] V. Kveder, W. Schröter, A. Sattler, and M. Seibt, *Mater. Sci. Eng. B* **71**, 175 (2000).
- [38] W. Schröter and H. Cerva, *Solid State Phenom.* **85/86** (2002).
- [39] V. Kveder, M. Kittler, and W. Schröter, *Phys. Rev. B* **63**, 115208 (2001).
- [40] C. Poisson, A. Rolland, J. Bernardini, and N. A. Stolwijk, *J. Appl. Phys.* **80**, 1 (1996).
- [41] A. Rodriguez, H. Bracht, and I. Yonenaga, *J. Appl. Phys.* **95**, 7841 (2004).